Photochemistry on the bottom side of the mesospheric Na layer

Tao Yuan[1,2], Wuhu Feng[3,4], John M. C. Plane[3], Daniel R. Marsh[3,5]

1. Physics Department, Utah State University, Logan, Utah, USA
2. Center for Atmospheric and Space Sciences, Utah State University, Logan, Utah, USA
3. School of Chemistry, University of Leeds, Leeds, UK
4. National Centre for Atmospheric Science, University of Leeds, Leeds, UK
5. National Center for Atmospheric Research, Boulder, Colorado, USA

Abstract

Lidar observations of the mesospheric Na layer have revealed considerable diurnal variations particularly on the bottom side of the layer where more than an order-of-magnitude increase of Na density has been observed below 80 km after sunrise. In this paper, multi-year Na lidar observations over a full diurnal cycle at Utah State University (USU) (41.8°N, 111.8°W) and a global atmospheric model of Na with 0.5 km vertical resolution in the mesosphere and lower thermosphere (WACCM-Na) are utilized to explore the dramatic changes of Na density on the layer bottom side. Photolysis of the principal reservoir $NaHCO_3$ is shown to be primarily responsible for the increase in Na after sunrise, amplified by the increased rate of reaction of $NaHCO_3$ with atomic H, which is mainly produced from the photolysis of H_2O and the reaction of OH with O_3. This finding is further supported by Na lidar observation at USU during the solar eclipse (> 96% totality) event on August 21st, 2017, when a decrease and recovery of the Na density on the bottom side of the layer were observed. Lastly, the model simulation shows that the Fe density below around 80 km increases more strongly and earlier than observed Na changes during sunrise because of the considerably faster photolysis rate of its major reservoir FeOH.

1. Introduction

The layer of Na atoms in the upper mesosphere and lower thermosphere (MLT, ~ 80-105 km in altitude), is formed naturally by meteoric ablation along with other metallic layers such as Fe, Mg, Ca and K [Plane et al., 2015]. The climatological variations of this Na layer are known to be mainly controlled by a series of chemical reactions and dynamics, including tides, gravity waves and the mean circulation in the MLT [Plane, 2004, Marsh et al., 2013]. Mesospheric Na atoms are an important tracer in the MLT, where they are observed by resonance fluorescence, either by the lidar technique [Krueger et

al., 2015] or solar-pumped dayglow from space [Fan et al., 2007]. The Na lidar technique has enabled high temporal and spatial resolution measurements of the mesospheric Na layer since the 1970s [Sandford and Gibson, 1970]. In addition to Na density observations, Na temperature/wind lidars can measure the atmospheric temperature and wind fields over the full diurnal cycle by observing Doppler broadening and shifting of the hyperfine structure of one of the Na D lines [Krueger et al., 2015]. Atmospheric observations have been complemented by laboratory kinetic studies of the important reactions which control both the neutral and ion-molecule chemistry of Na in the MLT [Plane, 1999; 2004; Plane et al., 2015], and the development of atmospheric models which satisfactorily reproduce seasonal observations over most latitudes [Plane, 2004; Marsh et al., 2013; Li et al., 2018]

However, less detailed work has been done to investigate the diurnal variations in Na density, especially on the bottom side of the layer where neutral chemistry dominates. Advances in lidar technology have enabled Na density observations over a full diurnal cycle [Chen et al., 1996; States and Gardner, 1999; Clemesha et al., 2002; Yuan et al., 2012]. Utilizing multi-year observations, Yuan et al. [2012] investigated the diurnal variation and tidal period perturbations of the Na density. These tidal Na perturbations were then used to estimate the tidal vertical wind perturbations [Yuan et al., 2014], showing that, although closely correlated with tidal waves and dominated by tidal wave modulations in the lower thermosphere, the Na diurnal and semidiurnal variations cannot be induced by tidal modulations alone. This is especially the case on the bottom side of the layer below ~ 90 km, where tidal wave amplitudes are relatively small (see Figure 5a and 5b in Yuan et al., 2012), implying that other mechanisms make a significant contribution to the diurnal variation of the Na layer bottom side.

Plane et al. [1999] recognized the important role of photochemical reactions for characterizing the bottom side of the Na layer, and then measured the photolysis cross sections of several Na-containing molecules – NaO, NaO_2, NaOH and $NaHCO_3$, which models show to be significant mesospheric reservoir species [Self and Plane, 2002, Marsh et al., 2013]. These cross sections, measured at temperatures appropriate to the MLT, were then used to calculate mesospheric photolysis rates:

$NaO + h\nu \rightarrow Na + O$	5.5×10^{-2} s^{-1}	R1
$NaO_2 + h\nu \rightarrow Na + O_2$	1.9×10^{-2} s^{-1}	R2
$NaOH + h\nu \rightarrow Na + OH$	1.8×10^{-2} s^{-1}	R3
$NaHCO_3 + h\nu \rightarrow Na + HCO_3$	1.3×10^{-4} s^{-1}	R4

These *direct* photochemical reactions release atomic Na during daytime. Furthermore, *indirect* photochemistry also plays a role. The photolysis of O_2, O_3 and H_2O [Brasseur and Solomon, 2005] lead to the production of H and O (R5 – R8), increasing their concentrations by more than 1 order of magnitude during daytime at an altitude around 80 km [Plane, 2003]. The daily variation of H is further facilitated by the reactions between HO_2 and O/O_3, which has strong diurnal variations.

$O_2 + h\nu \rightarrow 2O$	R5
$O_3 + h\nu \rightarrow O + O_2$	R6
$H_2O + h\nu \rightarrow H + OH$	R7
$OH + O \rightarrow H + O_2$	R8
$NaHCO_3 + H \rightarrow Na + H_2CO_3$	R9

Thus, H and O reduce these Na compounds listed above to atomic Na [Plane, 2004].

To demonstrate the effect of solar radiation on mesospheric Na layer, including R1-R8, Figure 1 shows the averaged Na density variation in the layer between 75 km and 105 km during a 6-hour period that straddles sunrise (from 3 hours before to 3 hours after sunrise) in the fall season (from August 20 to September 30). The results are based on 50 days of Na lidar observations at USU (41.8°N, 111.8°W) between 2011 and 2016. Figure 1 also includes the ratio profile between the Na density 3 hours after sunrise to that 3 hours before sunrise. The lidar observations clearly show that, while there is an overall Na density increase after sunrise below ~ 92 km, the increase at and below 80 km is much larger than

76 closer to the layer peak: the Na density increases by a factor of ~ 6 at 80 km and ~ 40 near 78 km,
77 whereas it is almost unchanged around ~ 95 km. The dramatic oscillation of the ratio below 78 km is due
78 to very low Na density before sunrise (usually below 1 cm^{-3}). Note that this ratio calculation for Na
79 density profiles 1 hour before and 1 hour after sunrise generates a similar ratio profile, which
80 demonstrated even larger ratio near 80 km, a factor of ~ 20. This implies very quick Na density
81 enhancement during the process of sunrise. This analysis therefore provides strong evidence for the
82 impact of photochemistry on the bottom side of the Na layer.

83 In this paper we compare the USU Na lidar diurnal cycle observations of the mesospheric Na
84 layer during a continuous 7-day campaign in fall 2012 with the Na density variation simulated by
85 NCAR's Whole Atmosphere Community Climate Model with Na chemistry (WACCM-Na) [Marsh et al.,
86 2013] for the USU location during the same period, in order to investigate quantitatively the role of
87 photochemistry on the Na layer. In addition, Fe density variation by the latest WACCM-Fe [Feng et al.,
88 2017] due to photolysis is also discussed to show the distinct feature of the Fe in the bottom side of the
89 main layer. The Na Lidar measurements made during the solar eclipse on August 21, 2017 in North
90 America are then used as a further robust test of the role of photolysis.

91 **2. Instrument and Model description**

92 The USU Na Temperature/Wind lidar system, originally developed at Colorado State University, has
93 been operating at the USU main campus since summer 2010. In addition to Na density observations,
94 neutral temperature and winds are also measured for the mesopause region (~80-110 km) [Krueger et al.,
95 2015]. The lidar return signals can be recorded in 150 m bins in the line-of-sight direction, and saved
96 every minute. Facilitated by a pair of customized Faraday filters deployed at its receiver [Harrell et al.,
97 2009], this advanced lidar system can also reject the sky background significantly during daytime, while
98 receiving the Na echo with minimum loss. This technique provides robust measurements of these
99 important atmospheric parameters under sunlight condition, thereby enabling this investigation of Na
100 photochemistry. In this study, we focus on two sets of Na lidar data: Na density data taken between UT

Day 271 (September 27) and UT Day 277 (October 3) of 2012 and lidar observations during the solar eclipse on August 21, 2017. The lidar observations presented here are processed with 2-km vertical resolution, and 10-minute and 30-minute temporal resolution for nighttime and daytime data, respectively, to achieve appropriate signal to noise (S/N) for studying the bottom side of the layer between 75 and 80 km, where the Na density is low (<100 cm^{-3}). The standard deviation of Na number density is ~ 10% to 40% between 85 and 95 km during this 7-day campaign. The lidar observations during the solar eclipse are processed with 10-minute resolution to investigate the potential eclipse-induced perturbations in detail.

WACCM-Na is a global meteoric Na model which satisfactorily reproduces lidar and satellite measurements of the Na layer [e.g., Marsh et al., 2013; Dunker et al., 2015; Plane et al., 2015; Langowski et al., 2017; Dawkins et al., 2016; Feng et al., 2017]. WACCM-Na uses the Community Earth System Model (version 1) framework [e.g., Hurrell et al., 2013], which includes detailed physical processes as described in the Community Atmosphere Model, version 4 (CAM4) [Neale et al., 2012], and has the fully interactive chemistry described in Kinnison et al. [2007]. The current configuration for WACCM is based on a finite volume dynamical core [Lin, 2004] for tracer advection. Water vapor in WACCM is prognostic and includes the source in the stratosphere from methane oxidation. The approximate water vapor concentration at the USU Na lidar site between 75 and 80 km on the day of the eclipse is 1-3 10^9 cm^-3 (equivalent to 3-5 ppmv). For the present study, we used a specific dynamics (SD) version of WACCM, in which winds and temperatures below 50-60 km are nudged towards NASA's Modern-Era Retrospective Analysis for Research and Applications (MERRA) [Lamarque et al., 2012]. The horizontal resolution is 1.9˚ latitude × 2.5˚ longitude. For this study we performed model experiments using two different vertical resolutions: 88 and 144 vertical model levels (termed as lev88 and lev144), both have the same 62 vertical levels from surface to 0.42 Pa (below ~50 km) as MERRA with different vertical resolutions above 0.42 Pa. Basically, lev88, which has been used as a standard SD-WACCM, gives a coarse height resolution from ~1.9 to ~3.5 km above the upper stratosphere to MLT, while lev144 increases the resolution from 1.9 km down to around 500 m in MLT [Merkel et al., 2009; Viehl et al.,

2016]. The Na reaction scheme described in Plane et al. (2015) is updated with the results of recent laboratory studies [Gomez-Martin et al., 2016; 2017], and the meteoric input function (MIF) of Na from Cárrillo-Sanchez et al. (2016) is used. Note that the absolute Na MIF used in this paper is the same as in Li et al. (2018) and Plane et al. (2018); i.e., it has been divided by a factor of 5 from the MIF in Cárrillo-Sanchez et al. [2016], to match the observations. In order to contrast the photochemical behavior of the Na layer bottom side with that of the Fe layer, a WACCM-Fe simulation was also performed. The model output was sampled over USU (41.8°N, 111.8°W) every thirty minutes (the model time step) then interpolated to the same observational period for the available lidar daytime measurements for direct comparisons (note that the modelled nighttime outputs use the same temporal resolution as that of the daytime results because the model time step is every 30 minutes, while the lidar nighttime measurement is every 10 minutes).

3. Comparison of the Na lidar observations with WACCM-Na

The averaged Na density diurnal variation calculated from the intensive 7-day USU Na lidar campaign is presented as the top plot in Figure 2. During the campaign, the time of sunrise in the MLT is around 06:56 local time (LT) based on solar elevation angle (-5° represents sunrise in the MLT); the noon and sunset times are 13:45 LT and 20:35 LT, respectively. The observations reveal strong variations within the layer during the day. Close to the layer peak there are three minima at around 20:00 LT (evening), 04:00 LT (right before dawn) and 16:00 LT (afternoon), where the Na density falls to ~ 3000/cm^3. These are separated by two significant maxima near 91 km: the stronger one occurs right after sunrise and lasts almost the whole morning with a peak density more than 4400/cm^3; the other maximum occurs near 22:00 LT (shortly before midnight), and has a much shorter lifetime (~ 1 hour) with peak density slightly above 4100/cm^3. Similar to Figure 1, on the bottom side of the main layer there is clear evidence of an increase of Na density after sunrise.

Compared with the lidar observations, Figure 2 (middle panel) shows that the relatively coarse resolution WACCM-Na produces a reasonable Na layer in terms of a peak Na density close to 4500 cm^{-3}.

However, in contrast to the lidar observations, three distinct features are observed: first, the maxima and minima around the layer peak are much less obvious; second, the peak height of the simulated Na layer is near 87 km, about 3-4 km lower than the lidar observations, partly due to a few km lower mesopause in SD-WACCM [Feng et al., 2013]; third, the absolute value of Na density vertical gradient below the layer peak is much larger than observed. For instance, the modeled Na density decreases from near 4500 cm^{-3} at 87 km to ~ 2000 cm^{-3} around 82 km, while a similar density decrease is observed by the lidar to occur between about 95 km and 82 km. Of course, the second and third differences are probably related. In contrast, Figure 2 (bottom panel) shows that the WACCM-Na high resolution (lev144) output does capture the three-minima at the layer peak during a diurnal cycle, as observed (Figure 2, top panel). Although the Na density near the first minimum (~ 4500 cm^{-3}) is higher than observed, the times of the minima, which are close to 20:00 LT, 05:00 LT and 14:00 LT, are in good accord with the lidar observations. However, the Na peak density (> 5500/cm^3), along with the overall Na column abundance, is considerably higher than measured by the lidar, and the differences in peak height and vertical density gradient still persist.

In order to examine the density variation on the bottom side of the layer in greater detail, Figure 3 compares the time-resolved variation of the partial Vertical Column Density (VCD) below 80 km, where the magnitude of variations is the largest, from the 7-day lidar observations in September 2012 and the two WACCM-Na simulations. The variation of solar zenith angle is also plotted. Here, due to the differences of absolute density among the data sets, each VCD is normalized to its maximum so that all can fit in one plot. There is excellent agreement between the measured and modeled rates of change in Na VCD around sunrise and sunset. The VCD reaches a maximum around midday and is then fairly constant in the afternoon. This is because, contrary to the scenario in troposphere, the solar intensity in the mesosphere is pretty constant during the day. During the night, the Na VCD gradually decays to a minimum immediately before sunrise. The WACCM lev144 simulation also captures better the observed rate of decrease of Na immediately after sunset. Note also that the rate of decrease after sunset is faster than the increase following sunrise. This is caused by the rapid decrease in the concentrations of O and H

at sunset, compared with their slower photochemical buildup (R5-R8) and the photolysis of Na reservoir species (R1-R4) after sunrise.

An interesting contrast can be made with the behavior of the bottom side of the mesospheric Fe layer, where considerable density variations due to photolysis have also been observed by Fe lidars within the similar altitude range [Yu et al., 2012; Viehl et al., 2016]. Also included in Figure 3 is the modeled variation of the Fe VCD between 75 and 80 km, using a lev144 simulation with WACCM-Fe, which has been validated against Fe lidar observations [Viehl et al., 2016]. Note that although the rate of decrease of the Fe VCD around sunset is almost identical to that of Na (because both species correlate with the falling O and H concentrations after sunset) the rate of increase at sunrise is significantly faster. The Fe VCD reaches 70% of its daytime maximum within about 1 hour, whereas the Na VCD takes more than 4 hours to reach the same percentage of its maximum.

4. Na variation during solar eclipse

During the solar eclipse on August 21 2017, the USU Na lidar conducted a special campaign to observe its potential impact on the MLT. The lidar beam was pointed to the north, 30° off zenith, and operated between 09:45 LT and 15:00 LT. Although this campaign was limited by poor sky conditions in the early morning and afternoon, it was able to cover the complete course of the solar eclipse and observe the MLT at the peak of the eclipse with more than 96% of totality at 11:34 LT. To our knowledge, these are the first lidar observation in the MLT during an eclipse.

The lidar-observed mesospheric Na density variations during the event are shown in Figure 4, and the temporal resolution is 10-minute. The averaged return signal between 200 and 220 km altitude per lidar Line-of-Sight (LOS) binning range (150 m) is treated as the sky background, which is also shown in Figure 4. The background variation indicates that at the USU location the eclipse began at 10:25 LT, peaked at 11:34 LT, and ended just before 13:00 LT. The high background before 10:00 LT was due to hazy sky condition in the early morning, similar to after 15:00 when it became cloudy. During the course of this event, the mesospheric Na layer weakened with decreasing peak density. In particular, Na density

variation was more evident below 85 km. As Figure 4 shows, before the eclipse the constant density lines on the bottom side of the layer were moving downwards (i.e. increasing density at each altitude). As the eclipse unfolded, these constant density lines started to move towards higher altitudes (the density decreased at each altitude). During the recovery phase of the eclipse, the Na density began to increase again. By ~ 13:00 LT, the Na layer was fully recovered, and no significant change was observed on the bottom side of the layer. For example, the density line of 450 cm^{-3} was near 80 km right before the eclipse started. It moved upward to near 81.5 km at the culmination of the event, before it went back and stayed near 80 km at the end of the event. A similar behavior can be seen in all constant density lines below 85 km. Further calculation of the lidar measured bottom side Na VCD (75-85 km) shows that it decreased by about 40% between 10:25 LT and 11:35 LT.

The simultaneous temperature and horizontal wind measurements during the eclipse, however, do not reveal apparent variations that can be associated with the event (not shown). For instance, the measured temperature change is within the daytime lidar measurement uncertainty (~ 5K with 20-minute and 4 km smoothing). The temperature change during the solar eclipse is expected to be that small when considering the general energy budget in the MLT. When the short-wave heating that dominates the daytime budget (mainly exothermic heating from atomic O recombination) is turned off [Brasseur and Solomon, 2005], infrared cooling due to CO_2 emission would lead to net cooling in the mesopause region. However, the magnitude of this cooling is only about 1 K/hour [Roble, 1995]. Thus, for a solar eclipse that only lasts for two hours with just a few minutes of totality, a noticeable temperature change should not occur. This result is consistent with a recent simulation of the eclipse using the WACCM-X model, which concluded that the temperature variation in the mesosphere would have been no more than 4 K [McInerney et al., 2018]. Furthermore, the variation of temperature within this range will not have a significant impact on the Na reaction kinetics and hence the Na atom density [Plane et al., 1999].

5. Discussion

The major reservoir for Na on the bottom side of the layer is $NaHCO_3$, which forms by three steps from Na atoms: oxidation of Na by O_3 to NaO; reaction with H_2O or H_2 to form NaOH; and recombination of NaOH with CO_2 [Plane et al., 2015; Gomez-Martin et al., 2017]. $NaHCO_3$ is converted back to Na either by photolysis (reaction R4), or by reaction with atom H in R9. The rate coefficient for this reaction, R9, is $k_9 = 1.84 \times 10^{-13}\ T^{0.78} \exp(-1014/T)$ cm^3 molecule^{-1} s^{-1} [Cox et al., 2001], which is 7.1 $\times 10^{-14}$ cm^3 molecule^{-1} s^{-1}. The typical daytime H concentration between 75 and 80 km is around 5×10^7 cm^{-3} [Plane et al., 2015], so the first-order rate of this reaction is $\sim 4 \times 10^{-6}$ s^{-1}, which is about 40 times slower than R4. Thus, photolysis of $NaHCO_3$, which has built up during the night, is responsible for ~98% of the increase in the Na VCD after sunrise (Figure 3). The excellent agreement between the laboratory-measured photolysis rate of $NaHCO_3$ [Self and Plane, 2002], and the observed increase of the Na VCD is strong evidence that $NaHCO_3$ is indeed the major Na reservoir on the bottom side of the Na layer. Indeed, as shown in Figure 5, the WACCM_Na simulated variations of Na, H and O, between local midnight and noon, are highly correlated in the upper mesosphere in the same 144-level run. Within the same region, the $NaHCO_3$ density decreases above 78 km after sunrise due to photolysis and the increases in H and O. Below this altitude, the change in $NaHCO_3$ is much smaller because the concentrations of O and H, despite increasing after sunrise, are too small to prevent any Na produced being rapidly converted back to $NaHCO_3$. This is because the initial oxidation step – the recombination reaction of Na with O_2 (which is a pressure-dependent) – becomes very fast below 78 km.

Based on the above discussion, a decrease of Na on the bottom side of the layer would be expected during the eclipse, because of the reduction in the photolysis rates (R1-R4) and atomic O and H. As shown in Figure 4, a decrease in the Na density below 85 km was indeed observed by the lidar during this period. However, the decrease in Na is relatively small when compared with the natural variability measured with the USU Na lidar during the morning hours (observed over 50 days of lidar data between August 20 and September 30 in 2011-2016), which can be as much as 60% between 75 and 85 km, and is mostly driven by atmospheric gravity wave modulations [Shelton et al., 1980]. The effect of the eclipse was modeled by driving a 1D model of the Na layer (0.5 km vertical resolution, 5 min time resolution)

253 [Plane, 2004] with the background atmospheric species (O_3, O, H etc.) from the WACCM-X simulation
254 of the eclipse [McInerney et al., 2018]. As shown in Figure 6, the modeled decrease in Na around 80 km
255 is within the natural variability and much less than the diurnal change in the layer bottom side because
256 the time when photolysis is significantly reduced during the eclipse is too short.

257 In terms of the mesospheric Fe layer, the major Fe reservoir in this region is most likely FeOH [Self
258 and Plane 2003; Plane 2004; Plane et al., 2015]. Similar to Na, the dominant Fe production processes
259 within the bottom half of the layer involve reaction with H and photolysis:

260 $FeOH + H \rightarrow Fe + H_2O$ $\quad 3.1 \times 10^{-10}\exp(-1264/T)$ cm^3 molecule^{-1} s^{-1} (R10)

261 $FeOH + h\nu \rightarrow Fe + OH$ $\quad 6 \times 10^{-3}$ s^{-1} (R11)

262 The rate coefficients of both these reactions are considerably higher than those of the analogous Na
263 reactions, particularly R11 which is faster than R4 by more than two orders of magnitude [Viehl et al.,
264 2016]. It is this feature which controls the more rapid appearance of Fe around 80 km after sunrise, as
265 shown in Figure 4. Note that this rapid increase has been previously observed by lidar [Viehl et al., 2016;
266 Yu et al., 2012].

267 **6. Conclusions**

268 Observations of the full diurnal cycle of the bottom side of the mesospheric Na layer reveal
269 substantial changes in Na density near and below 80 km, with more than an order-of-magnitude increase
270 after sunrise, while the change of Na density above 90 km during the same process is relatively slow. In
271 this study we show that this diurnal variation is largely driven by the photochemistry of the major
272 reservoir species $NaHCO_3$. This result is established by demonstrating reasonable agreement between
273 USU lidar observations of the Na layer below 80 km, and a whole atmosphere chemistry-climate model
274 which includes a comprehensive Na chemistry module (WACCM-Na). Indirect photochemistry, where
275 atomic H and O are produced by the photolysis of O_3, O_2 and H_2O, and these atoms then reduce Na
276 compounds ($NaHCO_3$, NaOH, NaO and NaO_2) back to Na, also plays an important role in the diurnal
277 variability. The more rapid increase of atomic Fe after sunrise, which has been observed in several

278 locations [Viehl et al., 2016; Yu et al., 2012], is consistent with the much faster rate of photolysis of
279 FeOH compared with $NaHCO_3$. Lidar observations made during the solar eclipse on August 21, 2017 (at
280 a location with 96% totality) did not reveal significant changes in either temperature or Na density that
281 were larger than the natural variability around 80 km. This is consistent with a recent study using
282 WACCM-X [McInerney et al., 2018] and the Na model results presented here.

283 **Data availability:**

284 The USU Na lidar data of this study are available at the Consortium of Resonance and Rayleigh
285 Lidars (CRRL) Madrigal data base at: http://madrigal.physics.colostate.edu/htdocs/.

286 **Author contribution:**

287 Dr. Tao Yuan has been responsible for the lidar operations and the associated experimental data
288 analysis that are related to this work. Dr. Feng conducted the numerical simulations using the WACCM-
289 Na and WACCM-Fe. Dr. John Plane and Dr. Marsh provided the chemical and atmospheric dynamic
290 theories for this collaborative work.

291 **Acknowledgement:**

292 The lidar work in this study was performed as part of a collaborative research program supported
293 under the CRRL National Science Foundation (NSF) grant AGS1135882, with additional support from
294 NSF grants AGS1734333, and N000141712149 of Naval Research Laboratory. The National Center for
295 Atmospheric Research is sponsored by the NSF. JMCP and WF acknowledge funding from the European
296 Research Council (project number 291332 - CODITA).

297 **Reference:**

298 Brasseur, G. P. and Solomon, S., Aeronomy of the Middle Atmosphere: Chemistry and Physics of the
299 Stratosphere and Mesosphere, Springer, New York, 2005.

300 Carrillo-Sánchez, J. D., D. Nesvorný, P. Pokorný, D. Janches, and J. M. C. Plane, Sources of cosmic dust
301 in the Earth's atmosphere, Geophys. Res. Lett., 43, 11,979–11,986, doi: 10.1002/2016GL071697, 2016.

302 Chen, H., M. A. White, D. A. Krueger, and C. Y. She, Daytime mesopause temperature measurements
303 using a sodium-vapor dispersive Faraday filter in lidar receiver, Opt. Lett., 21, 1003–1005, 1996.

304 Clemesha, D. M., P. P. Batista, D. M. Simonich, Tide-induced oscillations in the atmospheric sodium
305 layer, J. Atmos. Sol.-Terr. Phys., 64, 1321–1325, 2002.

306 Cox, R.M., D.E. Self and J.M.C. Plane, A study of the reaction between NaHCO3 and H: apparent
307 closure on the neutral chemistry of sodium in the upper mesosphere, Journal of Geophysical Research,
308 106, 1733-1739, 2001

309 Dawkins, E. C. M., J. M. C. Plane, M. P. Chipperfield, W. Feng, D. R. Marsh, J. Höffner, and D. Janches,
310 Solar cycle response and longterm trends in the mesospheric metal layers, J. Geophys. Res. Space
311 Physics, 121, 7153–7165, doi: 10.1002/2016JA022522, 2016.

312 Dunker, T., U.-P. Hoppe, W. Feng, J.M.C. Plane, D.R. Marsh, Mesospheric temperatures and sodium
313 properties measured with the ALOMAR Na lidar compared with WACCM, J. Atmos. Sol.-Terr. Phys.,
314 127, pp. 111-119, 2015.

315 Fan, Z. Y., J. M. C. Plane, J. Gumbel, J. Stegman, and E. J. Llewellyn, Satellite measurements of the
316 global mesospheric sodium layer, Atmospheric Chemistry and Physics, 7, 4107-4115, 2007.

317 Feng, W., D. R. Marsh, M. P. Chipperfield, D. Janches, J. Hoeffner, F. Yi, and J. M. C. Plane, A global
318 atmospheric model of meteoric iron, J. Geophys. Res. Atmos., 118, 9456–9474, 2013.

319 Feng, W., Bernd Kaifler, Daniel R. Marsh, Josef Höffner, Ulf-Peter Hoppe, Bifford P. Williams and John
320 M.C. Plane, Impacts of a sudden stratospheric warming on the mesospheric metal layers, J. Atmos. Sol.-
321 Terr. Phys., 10.1016/j.jastp.2017.02.004, 162, (162-171), 2017.

322 Gómez Martín, J. C., Garraway, S., Plane, J. M. C., Reaction Kinetics of Meteoric Sodium Reservoirs in
323 the Upper Atmosphere, Journal of Physical Chemistry A, 120, 1330-1346, DOI:
324 10.1021/acs.jpca.5b00622, 2016.

325 Gómez Martín, J. C., C. Seaton, M. P. de Miranda, and J. M. C. Plane, The Reaction between Sodium
326 Hydroxide and Atomic Hydrogen in Atmospheric and Flame Chemistry, The Journal of Physical
327 Chemistry A 2017 121 (40), 7667-7674, DOI: 10.1021/acs.jpca.7b07808, 2017.

328 Harrell, S. D., C. Y. She, T. Yuan, D. A. Krueger, H. Chen, S. Chen, and Z. L. Hu (2009), Sodium and
329 potassium vapor Faraday filters re-visited: Theory and applications, J. Opt. Soc. Am. B, 26(4), 659-670,
330 2009.

331 Hurrell, J. W., J. J. Hack, A. S. Phillips, J. Caron, and J. Yin, The dynamical simulation of the
332 Community Atmosphere Model version 3 (CAM3), J. Clim., 19, 2162–2183, 2006.

333 Kinnison, D. E., et al., Sensitivity of chemical tracers to meteorological parameters in the MOZART-3
334 chemical transport model, J. Geophys. Res., 112, D20302, doi:10.1029/2006JD007879, 2007.

335 Krueger, D. A., C.-Y. She and T. Yuan, Retrieving mesopause temperature and line-of-sight wind from
336 full-diurnal-cycle Na lidar observations, Applied Optics 54(32), pp. 9469-9489, 2015.

337 Lamarque, J.-F., Emmons, L. K., Hess, P. G., Kinnison, D. E., Tilmes, S., Vitt, F., Heald, C. L., Holland,
338 E. A., Lauritzen, P. H., Neu, J., Orlando, J. J., Rasch, P. J., and Tyndall, G. K.: CAM-chem: description
339 and evaluation of interactive atmospheric chemistry in the Community Earth System Model, Geosci.
340 Model Dev., 5, 369–411, doi:10.5194/gmd-5-369-2012, 2012.

341 Langowski, M. P., von Savigny, C., J. P. Burrows, D. Fussen, E. C.M. Dawkins, W. Feng, J. M. C. Plane,
342 and D. R. Marsh, Comparison of global datasets of sodium densities in the mesosphere and lower
343 thermosphere from GOMOS, SCIAMACHY and OSIRIS measurements and WACCM model
344 simulations from 2008 to 2012, Atmos. Meas. Tech., 10, 2989–3006, 2017 https://doi.org/10.5194/amt-
345 10-2989-2017, 2017.

Li, T., Ban, C., Fang, X., Li, J., Wu, Z., Feng, W., Plane, J. M. C., Xiong, J., Marsh, D. R., Mills, M. J., Dou, X., Climatology of mesopause region nocturnal temperature, zonal wind and sodium density observed by sodium lidar over Hefei, China (32°N, 117°E), Atmos. Chem. Phys., 18, 11683–11695, doi.org/10.5194/acp-18-11683-2018, 2018.

Lin, S.-J., A "vertically-Lagrangian" finite-volume dynamical core for global atmospheric models, Mon. Weather Rev., 132, 2293–2307, 2004.

Marsh, D. R., Janches, D., Feng, W., & Plane, J. M. C., A global model of meteoric sodium. Journal of Geophysical Research: Atmospheres, 118, 11,442–11,452. https://doi.org/10.1002/jgrd.50870, 2013.

McInerney, J. M., Marsh, D. R., Liu, H.-L., Solomon, S. C., Conley, A. J., & Drob, D. P., Simulation of the 21 August 2017 solar eclipse using the Whole Atmosphere Community Climate Model-eXtended. Geophysical Research Letters, 45, 3793–3800. https://doi.org/10.1029/2018GL077723, 2018.

Merkel, A. W., Marsh, D. R., Gettelman, A., and Jensen, E. J., On the relationship of polar mesospheric cloud ice water content, particle radius and mesospheric temperature and its use in multi-dimensional models, Atmos. Chem. Phys., 9, 8889-8901, https://doi.org/10.5194/acp-9-8889-2009, 2009.

Neale, R., J. Richter, S. Park, P. Lauritzen, S. Vavrus, P. Rasch, and M. Zhang, The mean climate of the Community Atmosphere Model (CAM4) in forced SST and fully coupled experiments, J. Clim., 26(14), 5150–5168, doi:10.1175/JCLI-D-12-00236.1, 2013.

Plane, J. M., C. S. Gardner, J. Yu, C. Y. She, R. R. Garcia and H. C. Pumphrey, Mesospheric Na layer at 40N: Modeling and observations, J. Geophys. Res., 104(D3), 3773-3788, 1999.

Plane, J. M. C., Atmospheric chemistry of meteoric metals, Chem. Rev., 103(12), 4963–4984, doi:10.1021/cr0205309, 2003.

Plane, J. M. C, A time-resolved model of the mesospheric Na layer: Constraints on the meteor input function. Atmospheric Chemistry and Physics, 4, 627–638. https://doi.org/10.5194/acp-4-627-2004, 2004.

370 Plane, J. M. C., et al. (2014), A combined rocket-borne and ground-based study of the sodium layer and
371 charged dust in the upper mesosphere, J. Atmos. Sol.-Terr. Phys., 118, 151–160, 2014.

372 Plane, J. M. C., W. Feng, and E. C. M. Dawkins, The mesosphere and metals: Chemistry and changes,
373 Chem. Rev., doi:10.1021/cr5, 2015.

374 Roble, R. G., Energetics of the mesosphere and thermosphere, R. M. Johnson, T. L. Killeen (Eds.), The
375 Upper Atmosphere and Lower Thermosphere: A Review of Experiment and Theory, American
376 Geophysical Union, Washington, DC, 1995.

377 Sandford, M. C. W., and A. J. Gibson, Laser radar measurements of the atmospheric sodium layer, J.
378 Atmos. Terr. Phys., 32, 1423-1430, 1970.

379 Shelton, J. D., C. S. Gardner, and C. F. Sechrist, Jr., Density response of the mesospheric sodium layer to
380 gravity wave perturbations, Geophys. Res. Lett., 7, 1069-1072, 1980.

381 Self, D. E. and J. M. C. Plane, Absolute photolysis cross-sections for $NaHCO_3$, NaOH, NaO, NaO_2 and NaO_3:
382 implications for sodium chemistry in the upper mesosphere, Phys. Chem. Chem. Phys., 4, 16-23, doi:
383 10.1039/B107078A, 2002.

384 Self, D. E., and J. M. C. Plane, A kinetic study of the reactions of iron oxides and hydroxides relevant to
385 the chemistry of iron in the upper mesosphere, Phys. Chem. Chem. Phys., 5, 1407–1418, doi:10.1039/
386 b211900e, 2003.

387 States, R. J., Gardner, C. S., Structure of mesospheric Na layer at 40N latitude: seasonal and diurnal
388 variations. J. Geophys. Res.,104, 11783-11798, 1999.

389 Viehl, T. P., J. M. C. Plane, W. Feng, and J. Höffner, The photolysis of FeOH and its effect on the
390 bottomside of the mesospheric Fe layer, Geophys. Res. Lett., 43, 1373–1381, doi:
391 10.1002/2015GL067241, 2016.

392 Yu, Z., X. Chu, W. Huang, W. Fong, and B. R. Roberts, Diurnal variations of the Fe layer in the
393 mesosphere and lower thermosphere: Four season variability and solar effects on the layer bottomside at
394 McMurdo (77.8°S, 166.7°E), Antarctica, J. Geophys. Res., 117, D22303, doi:10.1029/2012JD018079,
395 2012.

396 Yuan, T., She, C.-Y., Kawahara, T. D., & Krueger, D. A., Seasonal variations of mid-latitude
397 mesospheric Na layer and its tidal period perturbations based on full-diurnal-cycle Na lidar observations
398 of 2002–2008. J. Geophys. Res., 117, D1130, https://doi.org/10.1029/2011JD017031, 2012.

399 Yuan, T., She, C. Y., Oberheide, J., & Krueger, D. A., Vertical tidal wind climatology from full-diurnal-
400 cycle temperature and Na density lidar observations at Ft. Collins, CO (41°N, 105°W). J. Geophys. Res.:
401 Atmo., 119, 4600–4615, https://doi.org/10.1002/2013JD020338, 2014.

402

403 **Figure Captions:**

404 Figure 1. The Na density (cm^{-3}) variation between 75 km and 105 km in MLT during sunrise between
405 August 20th and September 30th (contour plot) in 2011-2016. Zero hour marks time of the sunrise at the
406 mesopause (bottom abscissa). The solid black profile is the ratio between the Na density 3 hours after
407 sunrise to that 3 hours before sunrise (its tick marks is plotted in top abscissa).

408 Figure 2. The averaged lidar measured Na density variation during the 7-day Na lidar campaign between
409 September 27 and October 3, 2012 (top); the Na density variations at USU location during the same time
410 frame simulated by WACCM_Na 88-level (middle) and 144-level (bottom).

411 Figure 3. The variations of Na VCD (75-80 km) measured the USU Na lidar during the 7-day Na lidar
412 campaign (asterisks), simulated by WACCM_Na 88-level run (orange dotted line) and 144-level run
413 (orange dashed line) and solar zenith angle (black long-dashed line), along with Fe VCD (75-80 km)
414 simulated by WACCM_Fe 144-level run (blue solid line).

Figure 4. The mesospheric Na density variation during the solar eclipse on August 21, 2017, observed by the Na lidar at Utah State University. The yellow solid line represents the lidar-detected sky background. The unit for the lidar background measurement is #photon/bin/minute.

Figure 5. The variations of Na (a), NaHCO3(b), H(c) and O(d) in the bottom side of the mesospheric Na layer, simulated by WACCM_Na_144-level run.

Figure 6. A 1D model simulation of the Na layer variation during the solar eclipse between 18:00 LT on August 20 and 18:00 LT on August 21 in 2017. The solar eclipse at the USU Na lidar location peaked at 11:34 on August 21 (marked by the solid arrow). The background atmospheric species (O_3, O, H etc.) are based on the outputs of WACCM-X eclipse simulation.

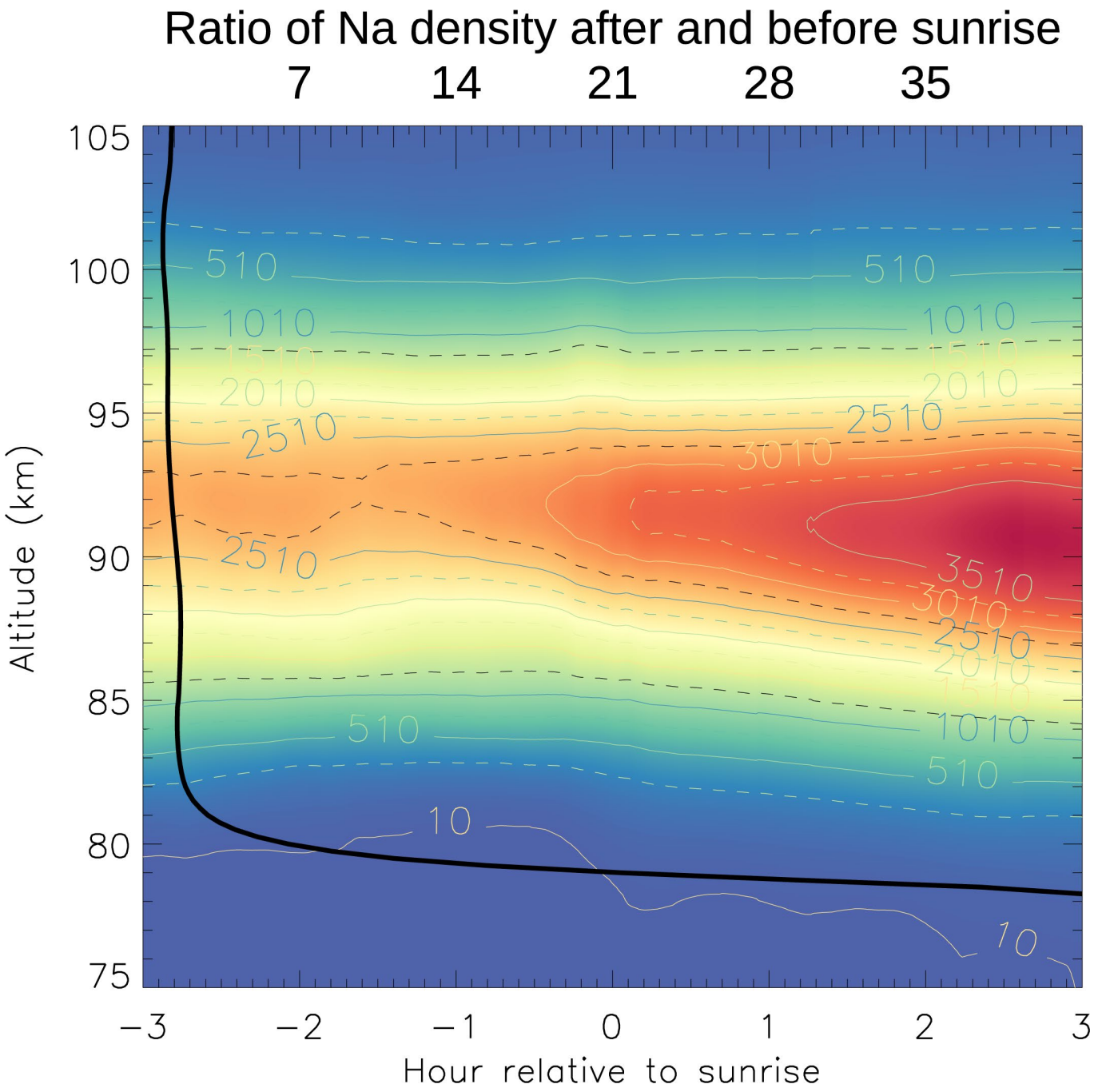

425

426 Figure 1. The Na density (cm^{-3}) variation between 75 km and 105 km in MLT during sunrise between

427 August 20th and September 30th (contour plot) in 2011-2016. Zero hour marks time of the sunrise at the

428 mesopause (bottom abscissa). The solid black profile is the ratio between the Na density 3 hours after

429 sunrise to that 3 hours before sunrise (its tick marks is plotted in top abscissa).

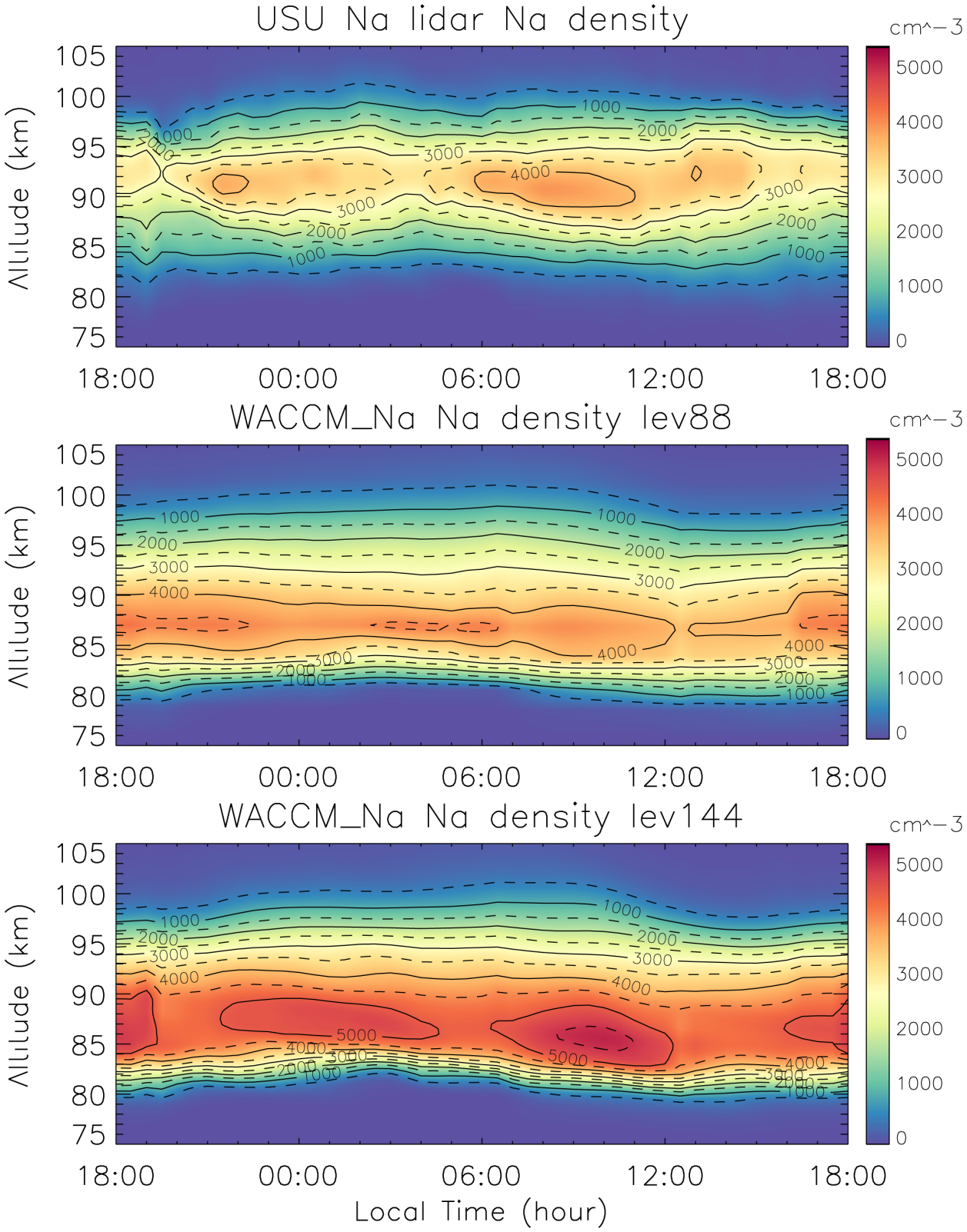

Figure 2. The averaged lidar measured Na density variation during the 7-day Na lidar campaign between September 27 and October 3 2012 (top); the Na density variations at USU location during the same time frame simulated by WACCM_Na 88-level (middle) and 144-level (bottom).

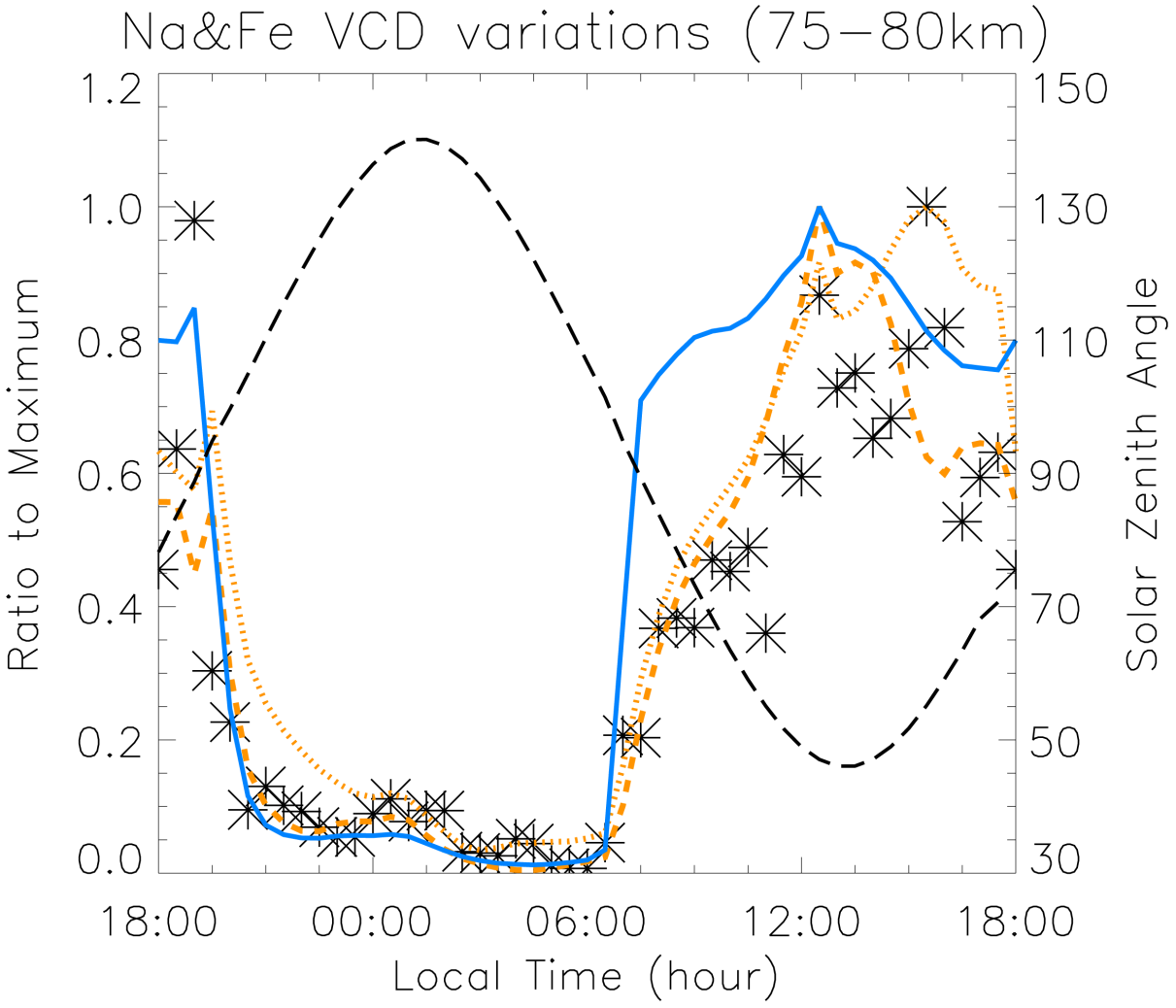

435

436 Figure 3. The variations of Na VCD (75-80 km) measured the USU Na lidar during the 7-day Na lidar
437 campaign (asterisks), simulated by WACCM_Na 88-level run (orange dotted line) and 144-level run
438 (orange dashed line) and solar zenith angle (black long-dashed line), along with Fe VCD (75-80 km)
439 simulated by WACCM_Fe 144-level run (blue solid line).

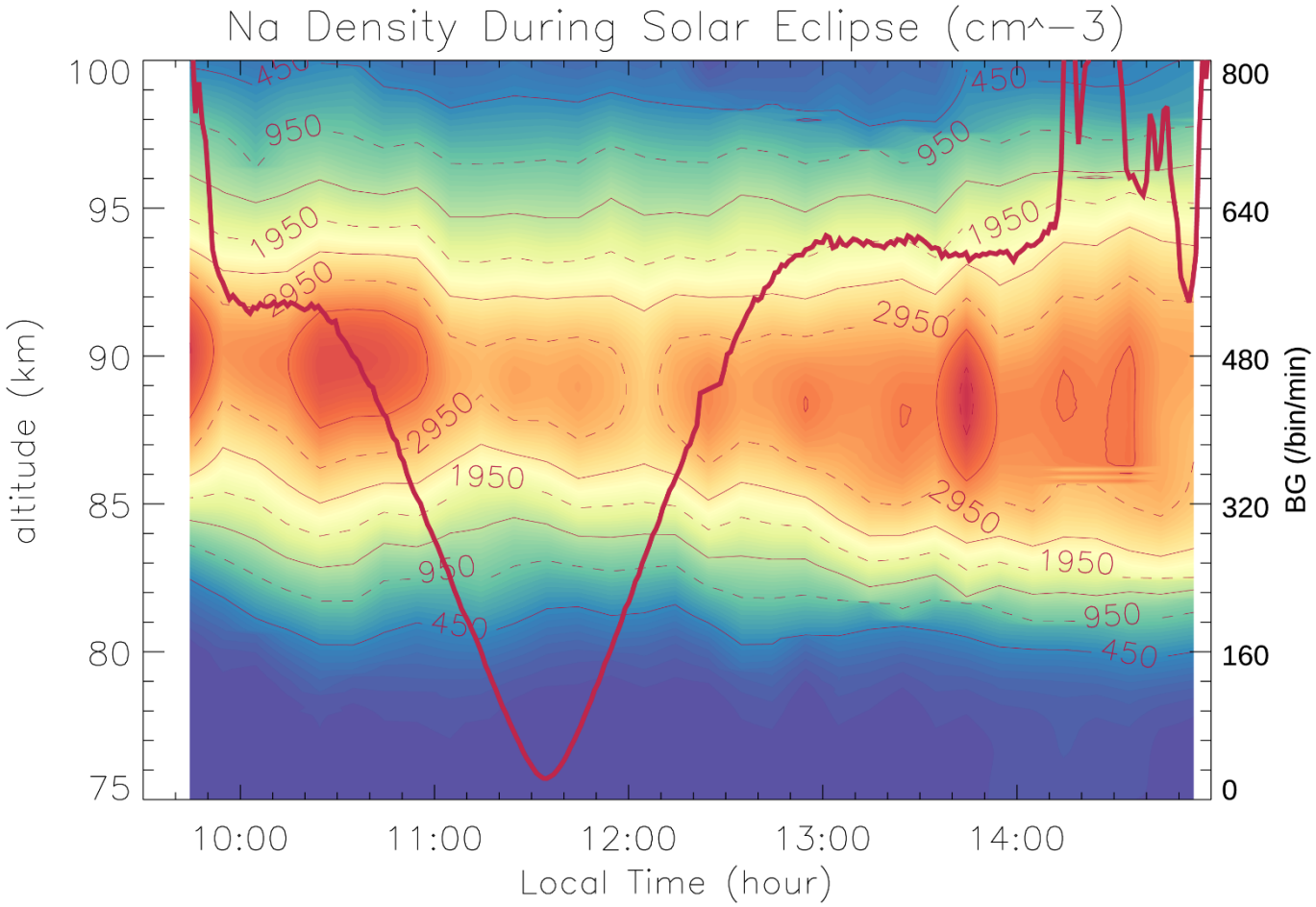

Figure 4. The mesospheric Na density variation during the solar eclipse on August 2, 2017, observed by the Na lidar at Utah State University. The red solid line represents the lidar-detected sky background. The unit for the lidar background measurement is #photon/bin/minute.

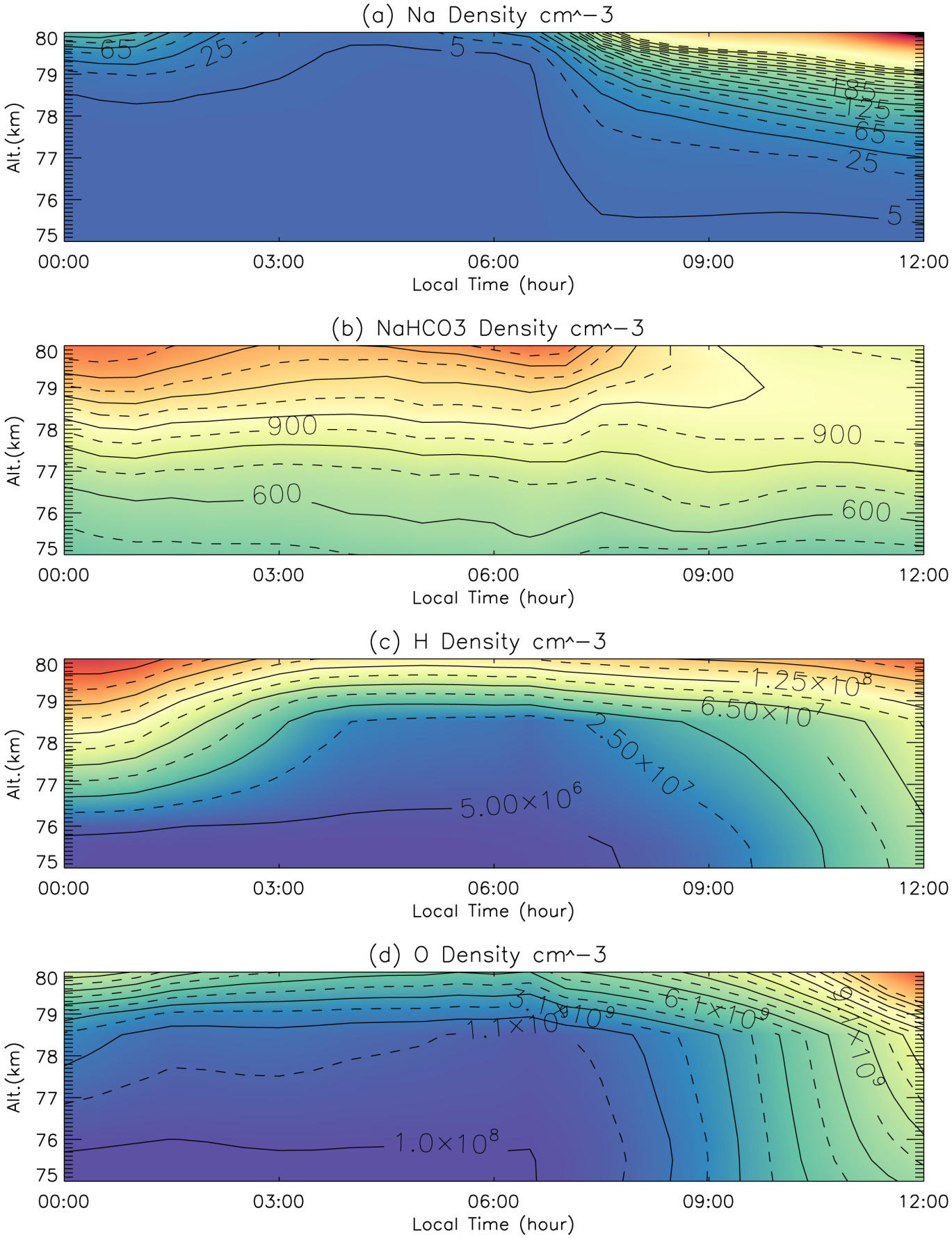
(a) Na Density cm^−3
65
25
5
185
125
65
25
5
(b) NaHCO3 Density cm^−3
900
600
900
600
(c) H Density cm^−3
1.25×10^8
6.50×10^7
2.50×10^7
5.00×10^6
(d) O Density cm^−3
3.1×10^9
1.1×10^9
6.1×10^9
1.0×10^8
Alt.(km)
80
79
78
77
76
75
00:00
03:00
06:00
09:00
12:00
Local Time (hour)

445

Figure 5. The variations of Na (a), $NaHCO_3$(b), H(c) and O(d) in the bottom side of the mesospheric Na layer, simulated by WACCM_Na_144-level run.

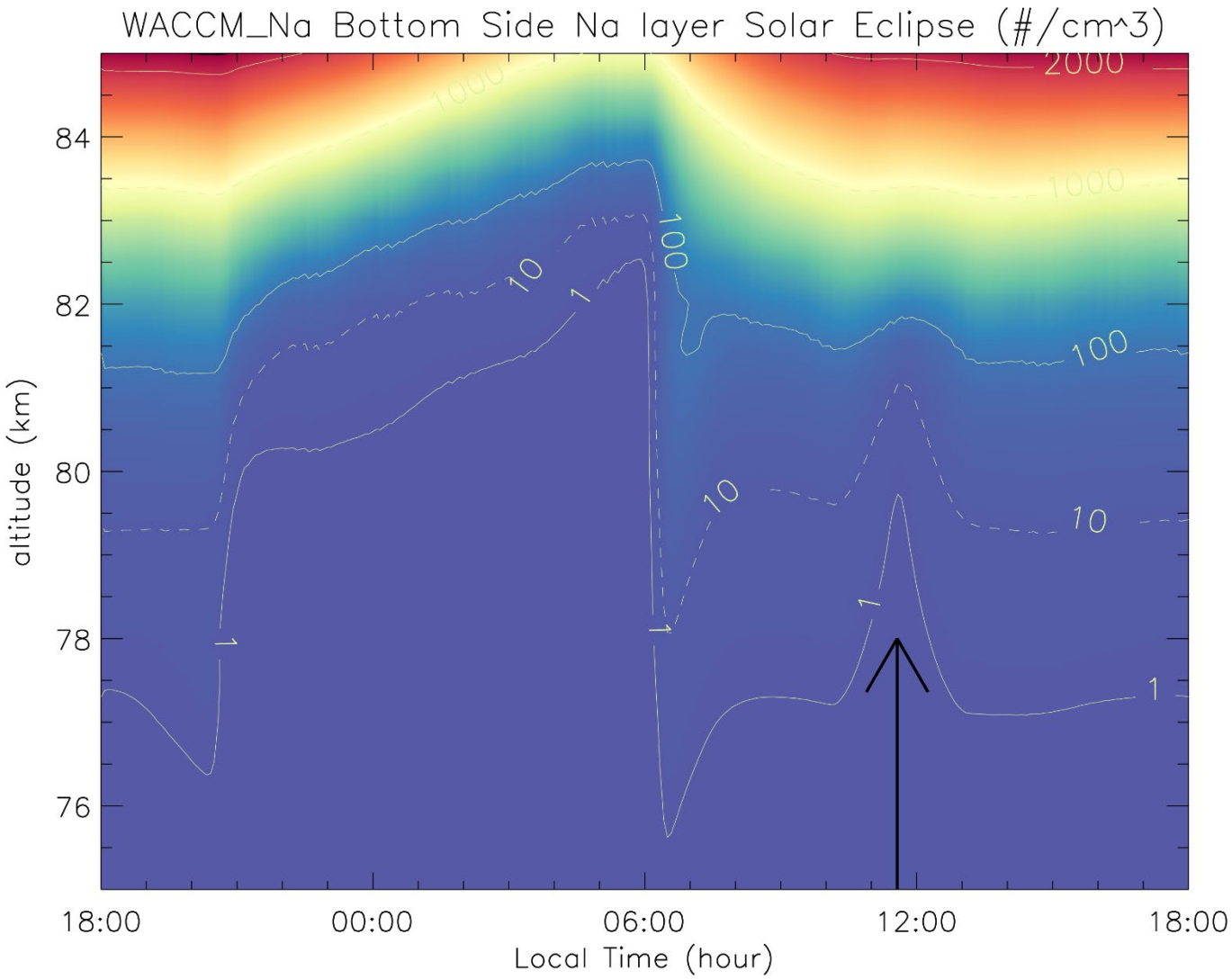

Figure 6. A 1D model simulation of the Na layer variation during the solar eclipse between 18:00 LT on August 20 and 18:00 LT on August 21 in 2017. The solar eclipse at the USU Na lidar location peaked at 11:34 on August 21 (marked by the solid arrow). The background atmospheric species (O_3, O, H etc.) are based on the outputs of WACCM-X eclipse simulation.